JBC RESEARCH ARTICLE

Truncation of the constant domain drives amyloid formation by immunoglobulin light chains

Received for publication, December 8, 2023, and in revised form, March 7, 2024 Published, Papers in Press, March 16, 2024,
https://doi.org/10.1016/j.jbc.2024.107174

Francesca Lavatelli[1,2,*], Antonino Natalello[3,*], Loredana Marchese[4], Diletta Ami[3], Alessandra Corazza[5,6], Sara Raimondi[1], Maria Chiara Mimmi[7], Silvia Malinverni[1], P. Patrizia Mangione[1,2], Manel Terrones Palmer[3], Alessio Lampis[1], Monica Concardi[7], Guglielmo Verona[1,8], Diana Canetti[8], Eloisa Arbustini[7], Vittorio Bellotti[2], and Sofia Giorgetti[1,2,*]

From the [1]Department of Molecular Medicine, Institute of Biochemistry, University of Pavia, Pavia, Italy; [2]Research Area, Fondazione IRCCS Policlinico San Matteo, Pavia, Italy; [3]Department of Biotechnology and Biosciences, University of Milano-Bicocca, Milan, Italy; [4]Pathology Unit, Fondazione IRCSS Policlinico San Matteo, Pavia, Italy; [5]Department of Medicine (DAME), University of Udine, Udine, Italy; [6]Istituto Nazionale Biostrutture e Biosistemi, Roma, Italy; [7]Transplant Research Area and Centre for Inherited Cardiovascular Diseases, Fondazione IRCCS Policlinico San Matteo, Pavia, Italy; [8]Centre for Amyloidosis, Division of Medicine, University College London, London, UK

Reviewed by members of the JBC Editorial Board. Edited by Ursula Jakob

AL amyloidosis is a life-threatening disease caused by deposition of immunoglobulin light chains. While the mechanisms underlying light chains amyloidogenesis *in vivo* remain unclear, several studies have highlighted the role that tissue environment and structural amyloidogenicity of individual light chains have in the disease pathogenesis. AL natural deposits contain both full-length light chains and fragments encompassing the variable domain (V_L) as well as different length segments of the constant region (C_L), thus highlighting the relevance that proteolysis may have in the fibrillogenesis pathway. Here, we investigate the role of major truncated species of the disease-associated AL55 light chain that were previously identified in natural deposits. Specifically, we study structure, molecular dynamics, thermal stability, and capacity to form fibrils of a fragment containing both the V_L and part of the C_L (133-AL55), in comparison with the full-length protein and its variable domain alone, under shear stress and physiological conditions. Whereas the full-length light chain forms exclusively amorphous aggregates, both fragments generate fibrils, although, with different kinetics, aggregate structure, and interplay with the unfragmented protein. More specifically, the V_L-C_L 133-AL55 fragment entirely converts into amyloid fibrils microscopically and spectroscopically similar to their *ex vivo* counterpart and increases the amorphous aggregation of full-length AL55. Overall, our data support the idea that light chain structure and proteolysis are both relevant for amyloidogenesis *in vivo* and provide a novel biocompatible model of light chain fibrillogenesis suitable for future mechanistic studies.

The hallmark of systemic amyloid diseases is the deposition of plasma proteins into interstitial amyloid fibrils (1). In systemic light chain (AL) amyloidosis, fibrillar precursors are monoclonal free immunoglobulin light chains (LCs) overexpressed in case of monoclonal gammopathies (2). Amyloid accumulation can affect virtually any tissue and results in severe organ dysfunction, dramatically impairing life expectancy and quality.

Immunoglobulin LCs consist of a constant domain (C_L) and a variable region (V_L), whose sequence is virtually unique for each patient and modulates the biochemical and biophysical properties of the protein (3, 4). Only a subset of LCs form amyloid *in vivo*, and, indeed, some patients with gammopathies do not develop fibrillar deposits even over a long period of time (5). The repertoire of AL LCs-germline genes is in fact skewed, with overrepresentation of the λ isotype and some subfamilies, mainly IGLV1-44, IGLV2-14, IGLV6-57, IGLV3-1, and IGKV1-33 (4, 6). The IGLV6-57 germline, specifically, is itself responsible for approximately one-fourth of all AL λ cases (4, 6, 7).

Treatment of AL amyloidosis is currently based on clonal plasma cells–directed chemotherapy, with the aim of reducing the abundance of the amyloidogenic precursor and preventing further fibril accumulation and proteotoxicity (8). Development of additional strategies for blocking early fibrillogenesis steps is complicated, since the pathogenic pathways underlying LC deposition *in vivo* are still largely unknown. On one hand, the LC variability prevents the identification of univocal sequence-related amyloidogenic features (9, 10). On the other hand, it is still unclear whether the full-length protein can itself aggregate in tissues, or whether proteolysis is required to generate specific amyloidogenic fragments that, after reaching a critical concentration, prime the formation of fibrils (11–13).

A key role for LCs fragmentation in the initiation of amyloid aggregation has been long debated (12–15). Structural evidence based on cryo-EM shows that the core of purified AL fibrils substantially consists of the V_L (16–18). In addition, whereas the full-length LCs from AL patients' are resistant to *in vitro* fibril formation, the corresponding isolated V_L rapidly converts into amyloid aggregates under physiological

* For correspondence: Francesca Lavatelli, francesca.lavatelli@unipv.it; Sofia Giorgetti, s.giorgetti@unipv.it; Antonino Natalello, antonino.natalello@unimib.it.

experimental conditions (12, 15, 19–24). This observation strongly suggests that the amyloidogenic potential of specific V_Ls can be disclosed after removal of C_L. *In vitro* evidence, indeed, supports the critical role of the C_L domain in modulating stability, dimerization, and aggregation of AL LCs (24–26). Coherently with the hypothesis that proteolysis of the constant domain may have a pathogenic role, AL LCs have been shown to be more susceptible to proteolysis compared to nonamyloidogenic ones (10, 12, 13, 27).

However, it is now clear that *ex vivo* amyloid deposits do not contain the V_L alone. The presence of full-length monoclonal LCs together with fragments containing both V_L and different length regions of the constant domain has been demonstrated over the years in several thousand clinical samples (14, 28–30). Proteomics has indeed revealed that the isolated V_L is only one among many LC fragments identified in the natural amyloid deposits (14, 29, 30). Understanding the role of these longer natural LC proteoforms in the pathogenesis of the disease is fundamental. Using mass spectrometry, we have recently characterized the cleavage sites in *ex vivo* ALλ amyloid deposits, showing that most of them fall in specific "hotspots" within the C_L (11, 31). While some cleavage sites may be compatible with postdeposition events, it remains unclear whether proteolysis within the hotspots in the constant region may release heterogeneous V_L-C_L fragments and whether they have a major role in amyloid fibril formation.

New models of *in vitro* fibrillogenesis are essential to understand the mechanisms driving the aggregation of LCs into fibrils and provide, at the same time, novel reliable tools for drug discovery. Previous work on isolated V_Ls has provided seminal information (19–23, 32–35); however, *in vitro* fibrillogenesis of V_L alone cannot mimic the biochemical features of natural amyloid. To establish more appropriate experimental models, we must take into consideration the simultaneous presence of both full-length and V_L-C_L fragments, with the aim of closing the existing gaps of knowledge between *in vivo* and *in vitro* evidence.

Therefore, based on previous characterization of *ex vivo* deposits related to LC AL-55, we have produced the full-length AL-55 protein together with its variable domain and a longer truncated species, whose C terminus is located in one of the previously identified cleavage hotspots (11, 14, 31). Our data show that the longer fragment, with its highly dynamic truncated C-terminal domain, is a major player in the formation of amyloid fibrils *in vitro*, supporting the role of proteolytic events within the C_L and suggesting that V_L-C_L fragments can contribute to LC fibrillogenesis in tissues. Our data provide a novel *in vitro* biocompatible model of LC fibrillogenesis that accounts for the contribution of the major proteoforms present in natural amyloid.

Results

Protein preparation

To study the role of full-length LC and LC proteolytic fragments of different length in amyloidogenesis, we have produced three recombinant proteins taking into consideration the natural pathogenic nonglycosylated AL55 LC sequence (11, 16, 31), belonging to the IGLV6-57 germline family. Based on the LC cleavage sites identified in *ex vivo* amyloid deposits, we have prepared three constructs encoding the corresponding recombinant species (Figs. 1*A* and S1): a) the full-length AL55 LC; b) the residue 1 to 133 fragment (133-AL55), which represented one of the *ex vivo* species identified in natural deposits (11, 31) and containing the V_L and 22 residues of the C_L; c) the V_L domain, comprising the 111 amino acids of the variable and joining regions (V_L-AL55).

Structural characterization and thermal stability

The secondary structure content of each species was assessed by far-UV CD spectra at 10 °C, a temperature at which the three proteins were stable (Fig. 1*B*). All spectra displayed a main minimum at around 218 nm, as expected for β-sheet–rich proteins. Spectral deconvolutions indicated an estimated β-sheet content of 42 to 45% (Fig. 1*C*) that was in line with what previously reported for full-length and V_L LCs (10, 25). We then assessed protein stability by collecting the CD signal at 203 nm at increasing temperatures (Fig. 1*D*, blue lines). While the full-length AL55 was stable up to 44 °C (midpoint temperature of 51.6 °C), V_L-AL55 and 133-AL55 were less stable with a midpoint temperature close to 38 °C (Fig. 1, *D* and *E*). Indeed, the CD spectra collected at 85 °C (Fig. 1*B*, red spectra) showed an increased random coil structure content for both the full-length and 133-AL55, as indicated by the main minimum at ∼203 nm. Minimum around 217 nm in the spectrum of V_L-AL55 suggested the presence of β-sheet–rich aggregates. The unfolding reversibility was assessed by cooling down the same samples to 10 °C, followed by a second thermal treatment from 10 to 85 °C (Fig. 1*D*, gray lines and S2). The stability monitored by the CD signal at 203 nm in the second thermal treatment (Fig. 1*D*, gray lines and S2) shows a conformational transition for 133-AL55 and V_L-AL55 species, although much less evident in the latter. Therefore, under these conditions, thermal unfolding was completely irreversible for the full-length LC, whereas the process was partially reversible for 133-AL55 and, to a much less extent, for V_L-AL55.

Further structural studies were carried out using AlphaFold2 (36). *In silico* predictions for the monomeric full-length AL55 and V_L-AL55 were in line with known structures determined for λ LCs and isolated V_Ls, containing, respectively, two and a single-structured domains with immunoglobulin fold. AlphaFold2 analysis for the 133-AL55 fragment was consistent with the existence of a defined structure in the corresponding V_L region and high residue flexibility in the remaining C_L sequence (Fig. 2*A*).

Molecular dynamics of 133-AL55 fragment

In addition to the AlphaFold2 prediction, solution NMR was performed to establish the actual 133-AL55 structure. The 2D [^{1}H-^{15}N] heteronuclear single quantum coherence (HSQC) spectrum of a 0.5 mM 133-AL55 in PBS at 37 °C (Fig. 2*B*) confirmed the simultaneous presence of well-dispersed cross-

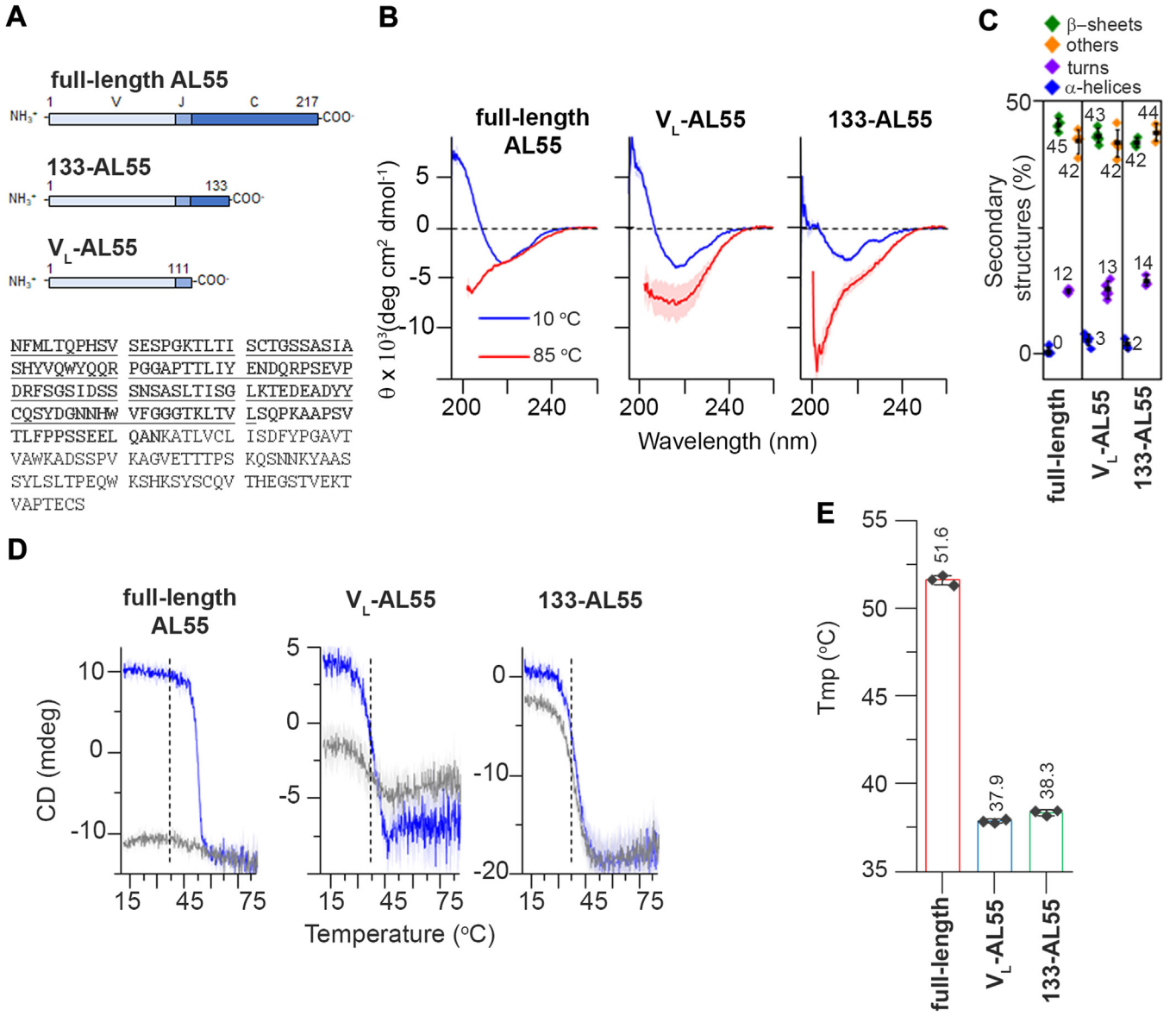

Figure 1. Sequence and conformational characterization of AL-55–related species. *A*, scheme of the three AL55 proteoforms under investigation with V (variable), J (joining), and C (constant) regions. Full-length sequence of AL55 shown in the *lower part of panel A* with highlighted sequences of 133-AL55 (in *bold*) and V_L-AL55 (*underlined*), respectively. *B*, far-UV CD spectra of the three AL55 species at pH 7.4, 10 °C, and 85 °C. *C*, secondary structure content of the three proteoforms based on far-UV CD spectra collected at 10 °C. *D*, thermal stability monitored by CD signal at 203 nm. After heating up to 85 °C (*blue lines*), samples were cooled down at 10 °C before repeating a second heating treatment (*gray lines*) to assess the reversibility of the temperature-induced conformational changes. *E*, temperature of the midpoint (Tmp). Values of Tmp for each species were determined from the corresponding curves reported in *E*. All data shown in *B–E* are expressed as mean and SD of three independent measurements. V_L, light chain's variable domain.

peaks indicative of a structured domain together with more intense peaks located in the middle of the spectrum, consistent with a nonstructured region. Under these conditions, the spectrum changed with time: the structured domain was no longer detectable after 6 h, evolving into a spectrum consistent with an unfolded/aggregated protein. When lowering the temperature to 15 °C, the conformational stability of 133-AL55 increased up to 32 h (Fig. S3), allowing to perform triple resonance 3D NMR experiments, required for backbone resonances assignment (Fig. 2*C*). Under these conditions, however, the 3D spectra allowed only partial assignment of the backbone amide peaks (19 out of 97 detectable peaks) in the [^{1}H-^{15}N] HSQC spectrum, due to lack of signal propagation. Interestingly, 14 of the 19 assigned peaks belonged to region 117 to 133 (C_L domain) and the remaining five were located in strand S4 and in the complementarity-determining region 2 loop; all the 19 assigned peaks exhibited chemical shifts typical of unfolded domains. The lack of signal propagation in 3D spectra affects 80% of the 133-AL55 residues all belonging to the V_L domain. This was consistent with various scenarios not predictable with *in silico* methods, such as the presence of multiple conformations or high molecular weight soluble aggregates. To further confirm the backbone dynamics of 133-AL55 in solution, we performed ^{1}H-heteronuclear Nuclear Overhauser Effect (^{1}H-{^{15}N} NOE) (37) spectroscopy at 15 °C. Data for the C_L assigned residues (Fig. 2*D*) show ^{1}H-{^{15}N}

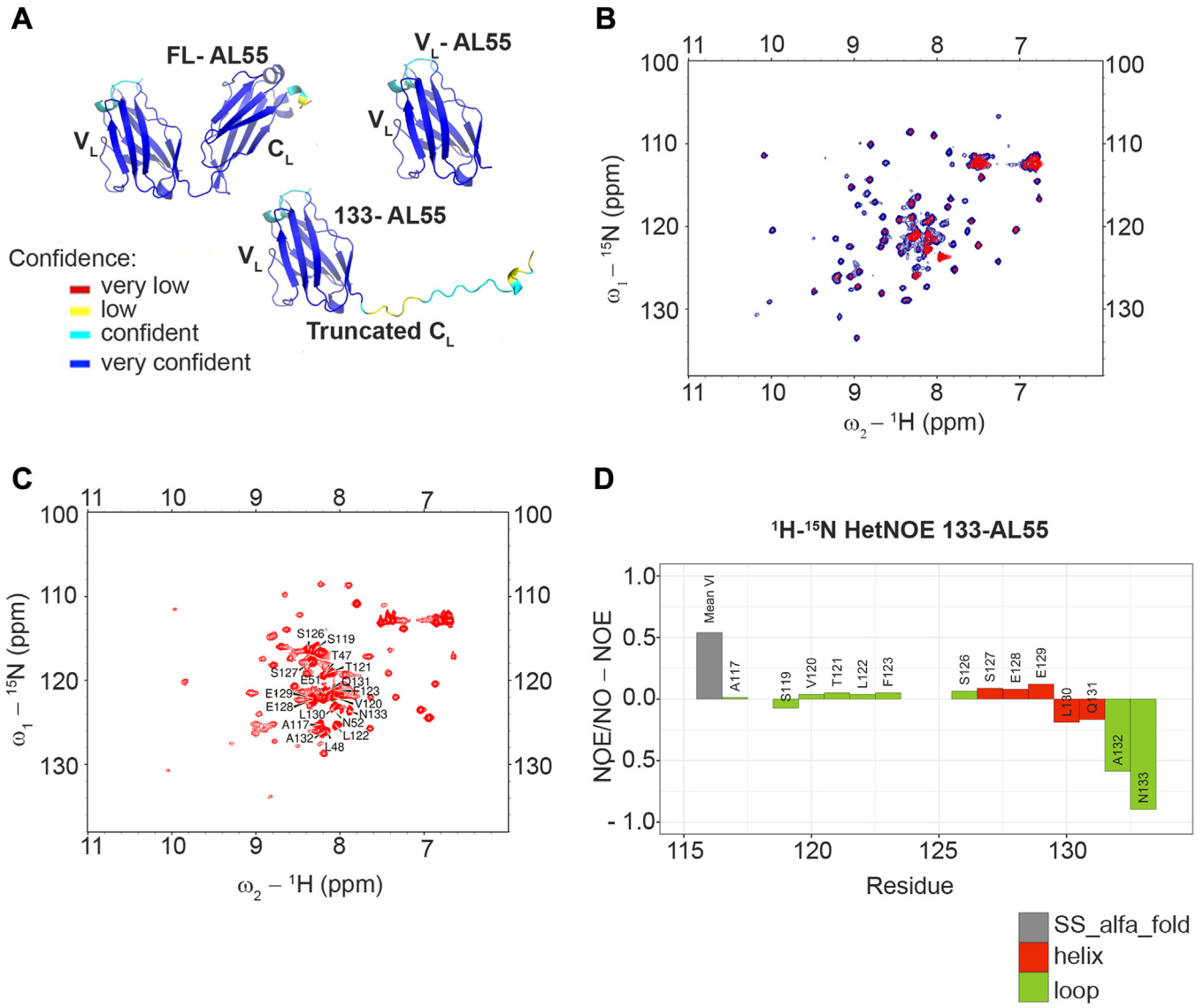

Figure 2. Structural evaluation of AL55 species. *A*, structures predicted using AlphaFold2. Residues in the 3D structures are colored according to their pLDDT value (AlphaFold per residue estimate of model confidence) with the following code: *red* pLDDT <50; *yellow* 50 ≤pLDDT <70; *cyan* 70 ≤pLDDT <90; *blue* pLDDT ≥ 90. *B*, conformational stability of 133-AL55 at 37 °C monitored by solution NMR. Superposition of the 2D [^{1}H-^{15}N] HSQC spectra of uniformly [^{13}C, ^{15}N] labeled 133-AL55 at 0.5 mM in PBS pH 7.4/D_2O, 95/5, vol/vol, recorded immediately after dissolution (*blue trace*) and after 6 h at 37 °C (*red trace*). *C*, 2D [^{1}H-^{15}N] HSQC spectrum of uniformly [^{13}C, ^{15}N] labeled 133-AL55 at 0.5 mM in PBS pH 7.4/D_2O, 95/5, vol/vol, recorded at 15 °C: the 19 assigned peaks (over 97 detectable peaks) are labeled. *D*, backbone dynamics of 133-AL55 investigated by ^{1}H-^{15}N heteronuclear NOE, at 15 °C on the same sample used for backbone resonances assignment. The ^{1}H-^{15}N NOE values are plotted *versus* sequential residue number for the 14 assigned amino acids belonging to the C_L domain and compared with the average of the remaining 59 peaks. C_L, light chain's constant domain; HSQC, heteronuclear single quantum coherence.

NOE values in the range of −0.9 to 0.12, whereas a typical value of 0.8 correlates with structured regions in which residues reorient along with the whole molecule.

Aggregation kinetics and mutual contribution of different species to fibril formation

The ability of the three proteins to convert into amyloid fibrils was explored by incubation at 37 °C in PBS pH 7.4, under agitation, and monitored by Thioflavin T (ThT) emission fluorescence (Figs. 3 and S4). Different agitation speeds and protein concentrations were tested. Whereas the full-length AL55 did not convert into amyloid fibrils over the entire observation time (up to 15 days, data not shown), both 133-AL55 and V_L-AL55 readily formed amyloid aggregates with disappearance of the soluble precursors from the supernatant within hours (Fig. S4*A*). However, their fibrillogenesis kinetics were different (Fig. 3, *A* and *B* and S4, *B*–*E*). Fibrillogenesis of V_L-AL55 was very fast and reached a ThT plateau within the first hour, independently on the agitation speed (Fig. S4*B*). In contrast, the lag phase of 133-AL55 was longer, and the rate of fibrillar growth was slower.

In addition, the maximum intensity of ThT fluorescence was higher for the 133-AL55 fragment than for V_L-AL55 (Fig. 3, *A* and *B*). The ThT curves of 133-AL55 varied with the agitation speed; in particular, at lower speeds, the lag phase

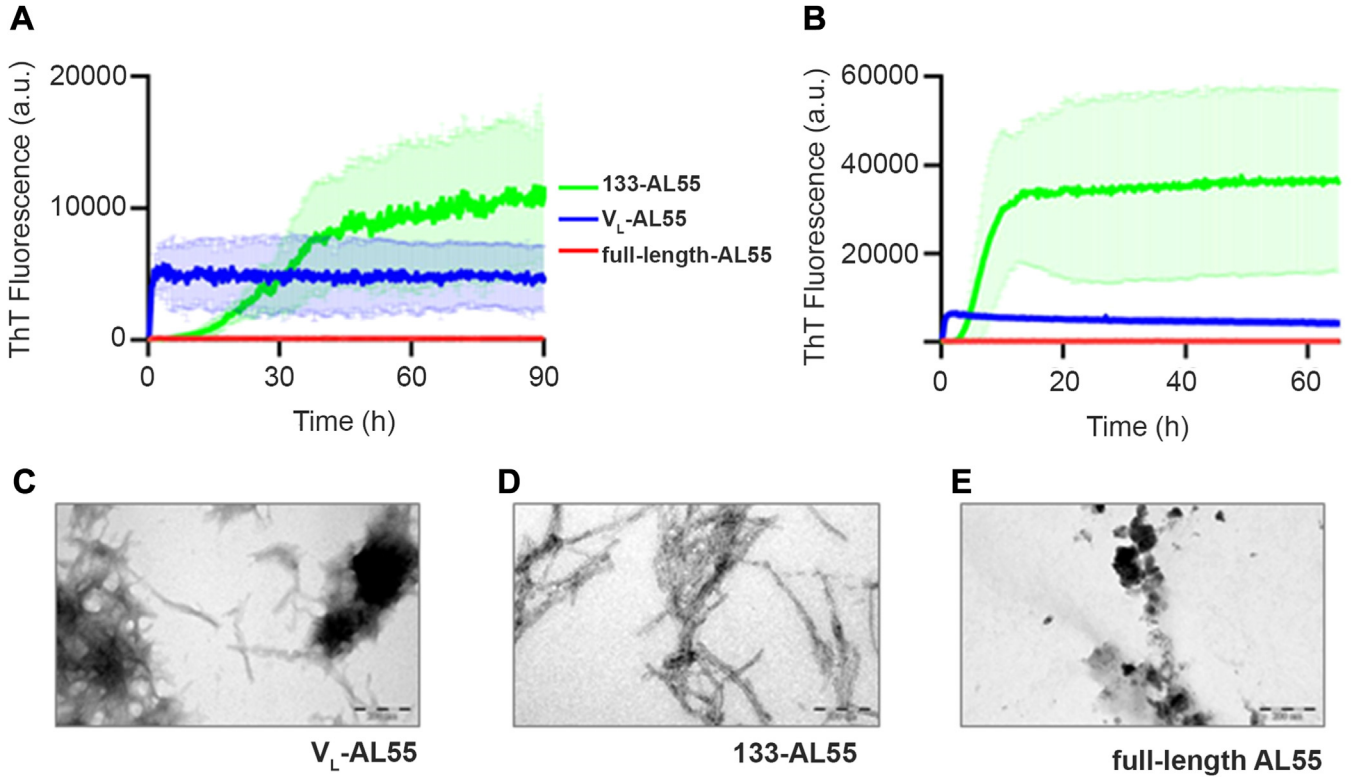

Figure 3. Fibrillogenesis of full-length AL55, 133-AL55, and V_L-AL55. *A*, ThT emission fluorescence monitored during incubation of each protein at 20 μM concentration, in the microplate assay format, using agitation speed at 100 rpm and (*B*), at 900 rpm. Shown V_L-AL55 (*blue*), 133-AL55 (*green*), full-length AL55 (*red*). *C–E*, representative TEM images of aggregates of V_L-AL55, 133-AL55, and full-length AL55, respectively. Samples were withdrawn after 48 h of incubation and directly applied onto the carbon grid (negative staining; the scale bars represent 200 nm). TEM, transmission electron microscopy; ThT, Thioflavin T; V_L, light chain's variable domain.

increased with reduction of the ThT value at plateau (Fig. S4*C*). Both species generated fibrils at low concentrations (down to 5 μM for V_L-AL55 and to 1 μM for 133-AL55, respectively), with a longer lag phase as the concentration decreased (Fig. S4, *D* and *E*). Morphology of the aggregates was studied using transmission electron microscopy (TEM) (Fig. 3, *C–E*), on samples directly applied onto the carbon grids without pelleting. Amyloid fibrils by both fragments were visible in the samples, whereas only amorphous aggregates were present in the case of the full-length, without detectable fibrillar or oligomeric species (Fig. 3*E*). Insoluble material obtained from V_L-AL55 also included significant amounts of amorphous aggregates (Figs. 3*C* and S4*F*), whereas the 133-AL55 sample contained almost only fibrillar species (Figs. 3*D* and S4*F*).

We then sought to study the fibrillogenesis process when both the full-length precursor and one of the amyloidogenic fragments were present in solution. To this aim, we mixed equimolar concentrations of full-length and either soluble 133-AL55 or V_L-AL55, at 37 °C, under agitation. Data indicate a substantially different scenario between the two mixtures. Coincubation of full-length AL55 with V_L-AL55 resulted in a ThT signal overlapping with that observed for the V_L-AL55 alone (Fig. 4*A*), suggesting no significant effect of V_L-AL55 on full-length aggregation. On the contrary, coincubation of full length with 133-AL55 significantly altered the kinetic profile compared to 133-AL55 alone, with extension of the lag phase and decrease in slope (Fig. 4*B*). T_{50} values for 133-AL55 alone and in the presence of the full-length protein are significantly different (respectively, 7.6 h *versus* 12.6 h; $p = 0.002$). Apparently, this unexpected and almost paradoxical effect of the fibrillogenesis rate inhibition did not influence the yield in fibrillar products, since the ThT value at the steady state was identical to that obtained by 133-AL55 alone.

Misfolding dynamics of the three different species during aggregation

The conformational changes during protein aggregation were monitored by FTIR spectroscopy (Figs. 5 and S5) in which β-sheet structures can be detected in native proteins and aggregates (38–40). Absorption spectra of each species in their native state (Fig. S5*A*) shows the amide I and amide II bands, which are mainly associated with the C=O stretching and N-H bending vibrations of the peptide bond, respectively (38). To resolve the overlapped components, the second derivative analyses were also performed. In particular, all the three species displayed two main amide I peaks at ~1691 cm^{-1} and ~1638 cm^{-1}, both assigned to the anti-parallel β-sheet structures of the proteins in their native state (38–41). To determine the individual contribution of different species in mixtures, as required in the cofibrillogenesis experiments, absorption spectra of isotopically labeled [^{13}C]full-length AL55 were acquired for isotope-

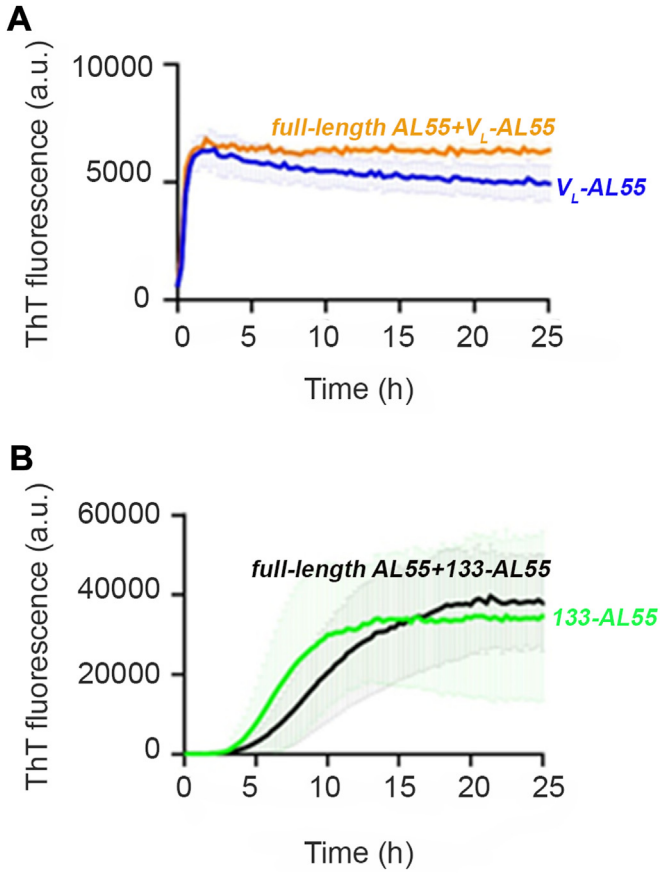

Figure 4. Fibrillogenesis of 133-AL55 or V_L-AL55 in mixture with full-length AL55. *A*, ThT emission fluorescence of full-length AL55 incubated with equimolar concentration of soluble V_L-AL55 monitored with time (*orange*). ThT signal of V_L-AL55 is shown in *blue*. *B*, ThT emission fluorescence of full-length AL55 incubated with equimolar concentration of soluble 133-AL55 monitored with time (*black*). ThT signal of 133-AL55 alone is shown in *green*. T_{50} values are significantly different (respectively, 7.6 h for 133-AL55 alone *versus* 12.6 h for 133-AL55 in the presence of the full length; $p = 0.002$; Student's *t* test). All incubations were carried out using 20 μM protein concentrations in microplates under agitation at 900 rpm. Curves shown as mean and SD of three independent experiments. ThT, Thioflavin T; V_L, light chain's variable domain.

edited FTIR analysis (42). Indeed, the replacement of ^{12}C with ^{13}C leads to a downshift of the IR components enabling us to study the conformational properties of [^{13}C] full-length AL55 in the presence of [^{12}C]V_L or [^{12}C]133-AL55 as IR peaks occur at a different spectral position for the labeled and unlabeled protein, respectively (Fig. S5*A*). However, for consistency, FTIR spectra of [^{13}C]full-length AL55 are reported both for the aggregation of the protein alone and in mixture. In the unfractionated sample of [^{13}C] full-length AL55, the native β-sheets related peak at ∼1596 cm^{-1} slowly decreased in intensity during incubation (Fig. 5*A*), and a new amide I component at around 1584 cm^{-1} was attributed to the formation of intermolecular β-sheets as a result of protein aggregation. This latter peak reached an intensity lower than that of the native β-sheets at the end of our observation (144 h), consistent with a partial protein aggregation. In this time frame, the native component at 1649 cm^{-1} gradually upshifted to 1650 cm^{-1}. Accordingly, the FTIR spectra of the supernatant after centrifugation displayed the features of native full-length AL55 at all investigated time points (24, 48, 72, and 144 h, Fig. 5*A*, middle spectra), whereas spectra of the pellet confirmed the presence of two main components at ∼1650 cm^{-1} and ∼1584 cm^{-1} (Fig. 5*A*, bottom spectra), assigned to intermolecular β-sheets typical of aggregates. The high noise in the second derivative spectra at 24 and 48 h was due to the low amount of protein in the pellet at these time points (Fig. 5*A*). In the V_L-AL55 sample, the native β-sheet components at ∼1691 cm^{-1} and ∼1638 cm^{-1} disappeared after 1 h, with appearance of two new peaks at ∼1696 cm^{-1} and ∼1622 cm^{-1}, assigned to intermolecular β-sheets (38, 40, 43) which reached a constant intensity after ∼1 h until the end of our observation (Fig. 5*B*). The complete aggregation of V_L-AL55 was confirmed by the disappearance of the protein from the supernatant spectra (data not shown) and the presence of intermolecular β-sheets related FTIR signals in the pellet (Fig. 5*B*, bottom spectra). Morphology of the V_L-AL55 aggregates was then confirmed with TEM (Fig. 3). The FTIR analysis of 133-AL55 sample indicated loss of the native β-sheet structures between 3 and 24 h (Fig. 5*C*). Indeed, the two peaks at ∼1691 cm^{-1} and ∼1638 cm^{-1} disappeared during this time frame, while intensity of new components at ∼1669 cm^{-1}, ∼1629 cm^{-1}, and ∼1617 cm^{-1} raised, implying a structural transition from the native antiparallel β-sheets to parallel β-sheet structures in the 133-AL55 amyloid derived fibrils (42, 44). Complete aggregation of this species was confirmed by the absence of the protein IR signal in the supernatant spectra (data not shown), while the pellet displayed the typical IR response of amyloid fibrils (components at ∼1669 cm^{-1}, ∼1629 cm^{-1}, and ∼1617 cm^{-1}; bottom spectra in Fig. 5*C*). Overall, the FTIR results were consistent with fibrillogenesis data monitored by ThT fluorescence.

Aggregation of [^{13}C]full-length AL55 in the presence of unlabeled V_L-AL55 was monitored by isotope-edited FTIR analysis (Fig. 6*A*). At the beginning of incubation, the [^{13}C]full-length AL55 with V_L-AL55 mixture (Fig. 6*A*) displayed the IR components assigned to the native β-sheets structures. Peaks of native V_L-AL55 disappeared during the first hour of incubation, in parallel with the appearance of the two components assigned to the V_L-AL55 aggregates (at ∼1696 cm^{-1} and ∼1622 cm^{-1}), and similarly to what observed for V_L-AL55 alone. At longer incubation times, the native [^{13}C]full-length AL55 component at ∼1596 cm^{-1} decreased in intensity and the intermolecular β-sheet peak at ∼1584 cm^{-1} raised. Accordingly, analysis of the supernatant collected at different time points (24, 48, 72, and 144 h respectively) showed the presence of [^{13}C]full-length AL55 in native-like secondary structures (Fig. 6*A*, middle spectra). In addition to the IR components assigned to the V_L-AL55 in the pellet, the peak of [^{13}C]full-length AL55 aggregates was also observed, with a relative intensity that increased with the incubation times (Fig. 6*A*, bottom spectra). In the mixture of [^{13}C] full-length AL55 with 133-AL55 (Fig. 6*B*), the IR components of the native fragment (at ∼1691 cm^{-1} and at ∼1638 cm^{-1}) decreased in intensity with slower kinetics than the 133-AL55 alone (Fig. 6, *C* and *D*). The IR signal of native [^{13}C]full-length AL55 in the supernatant was predominant in the spectra at 24,

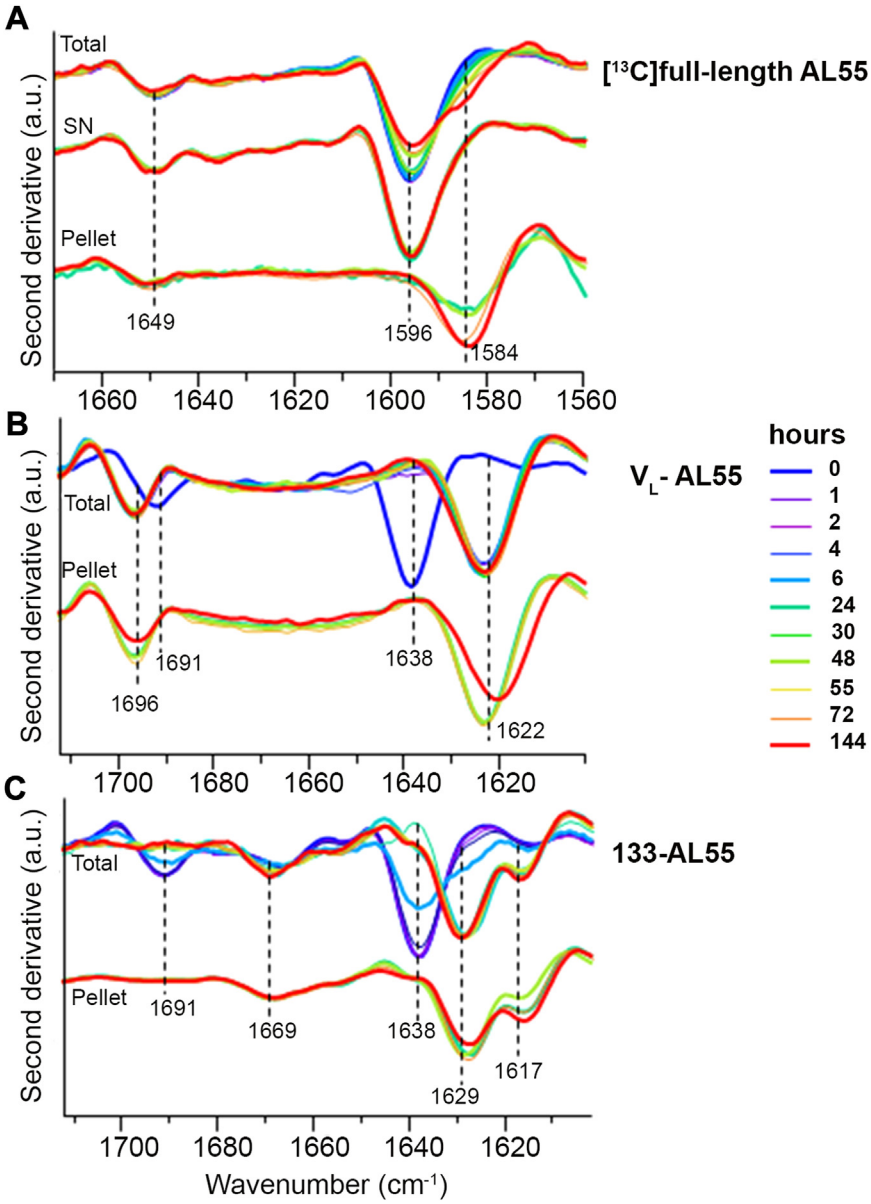

Figure 5. Fibrillogenesis of [^{13}C]full-length AL55, V_L-AL55, and 133-AL55 studied by FTIR spectroscopy. *A–C*, second derivatives of the FTIR absorption spectra of [^{13}C]full-length AL55 (*A*), V_L-AL55 (*B*), and 133-AL55 (*C*) collected at different incubation times. At 24, 48, 72, and 144 h of incubation at 37 °C, 20 μl aliquots of each sample were withdrawn and the FTIR spectra of supernatants (SN, *middle spectra* in *panel A*) and pellets (*bottom spectra* in all panels) were acquired. Representative spectra with the main peak positions are shown. V_L, light chain's variable domain.

48, 72, and 144 h, respectively (Fig. 6*B*, middle spectra). In addition to the IR components of the 133-AL55 fibrillar sample (at ∼1669 cm^{-1} and at ∼1629 cm^{-1}) in the pellet, the peaks of [^{13}C]full-length AL55 aggregates (at ∼1650 cm^{-1} and at ∼1584 cm^{-1}) were also observed, with a relative intensity that increased with the incubation time (Fig. 6*B*, bottom spectra). Analysis of spectra of [^{13}C]full-length AL55 in mixture with the 133-AL55 fragment at 144 h showed that a larger fraction of [^{13}C]full-length AL55 was misfolded in comparison with [^{13}C] full-length AL55 alone (Figs. 5*A* and 6*C*), as also confirmed by the very low concentration of protein in the supernatant at the last incubation time (Fig. 6*B*, middle spectra).

Pellets and supernatants were withdrawn after 48 h from the two mixtures, were also evaluated by SDS-PAGE (Fig. 7, *A* and *B*). In agreement with the FTIR data, both the 133-AL55 and V_L-AL55 species almost completely disappeared from the supernatant at 48 h, whereas the full-length AL55 was split up between supernatant and pellet in the corresponding electrophoretic bands. When examining the samples by electron microscopy (EM) (Fig. 7, *C* and *D*), coexistence of amyloid fibrils and amorphous aggregates was visible in both cases at both time points, although the nonfibrillar aggregates were morphologically different.

In addition, in cross-seeding experiments neither 133-AL55 nor V_L-AL55 seeds were able to recruit the full-length protein into ThT-positive aggregates (Fig. S6). In contrast, the kinetics of 133-AL55 was accelerated in the presence of homologous seeds (Fig. S6*A*), whereas the very fast kinetics of fibrillogenesis of the shorter fragment V_L-AL55 was not affected by its own seeds (Fig. S6*B*).

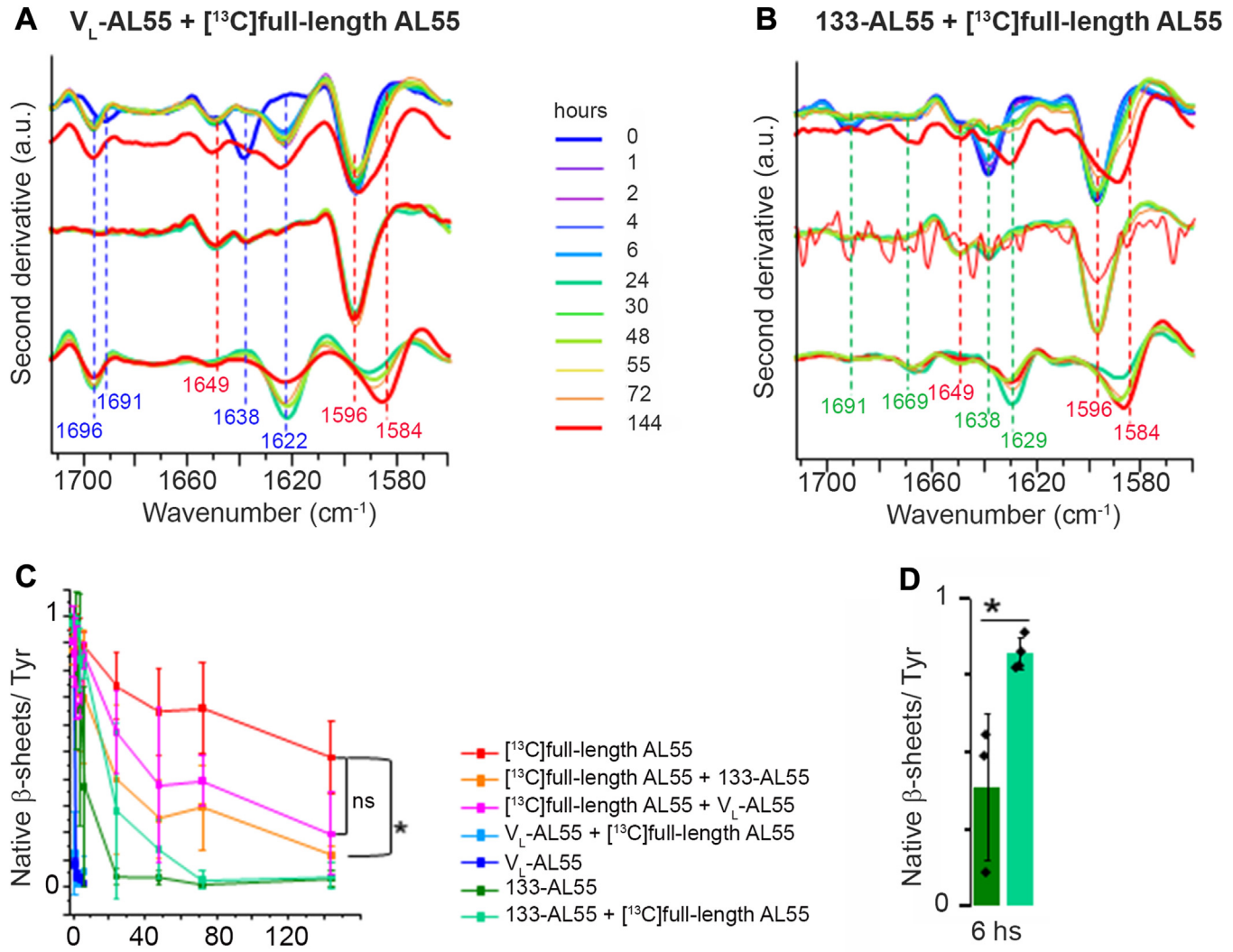

Figure 6. Fibrillogenesis of 133-AL55 or V$_L$-AL55 in mixture with [^{13}C]full-length AL55 by isotope-edited FTIR. *A*, second derivatives of the absorption spectra of samples containing both [^{13}C]full-length AL55 and unlabeled V$_L$-AL55 at different times of incubation at 37 °C. Representative spectra with main peak positions assigned to [^{13}C]full-length AL55 (*red numbers*) and V$_L$-AL55 (*blue numbers*) are reported. *B*, second derivatives of the absorption spectra of samples containing both [^{13}C]full-length AL55 and unlabeled 133-AL55 at different times of incubation at 37 °C. Representative spectra with main peak positions assigned to [^{13}C] full-length AL55 (*red numbers*) and 133-AL55 (*green numbers*) are shown. At 24, 48, 72, and 144 h of incubation, FTIR spectra of supernatants and pellets were also acquired and shown in *A* and *B panels*. *C*, time course aggregation monitored with the ratio of the IR peak assigned to the native β-sheets of each variant to the tyrosine peak, based on the second derivative spectra. The ratio was calculated for the following samples: [^{13}C] full-length AL55 (intensity at ∼1596 cm^{-1}/intensity at ∼1480 cm^{-1}) alone (*red*) and in the presence of V$_L$-AL55 (*magenta*) or 133-AL55 (*orange*); V$_L$-AL55 (intensity at ∼1638 cm^{-1}/intensity at ∼1516 cm^{-1}) alone (*blue*) and in the presence of [^{13}C] full-length AL55 (*light blue*); 133-AL55 (intensity at ∼1638 cm^{-1}/intensity at ∼1516 cm^{-1}) alone (*blue*) and in the presence of [^{13}C] full-length AL55 (*light blue*). *D*, intensity ratios for 133-AL55 alone (*green bar*) and in the presence of [^{13}C] full-length AL55 (*light green bar*) are shown as mean and SD of three independent experiments. *$p <$ 0.05, Student's *t* test. V$_L$, light chain's variable domain.

Discussion

Several factors concur to enable the transition from globular proteins to amyloid fibrils (45). Experimental evidence suggests that proteolysis is one of the major posttranslational modifications contributing to amyloid conversion of globular proteins *in vivo* (12, 13, 15). In order to clarify the role of truncated species of monoclonal LCs in AL amyloidosis, we have scrutinized folding dynamics and aggregation properties of 133-AL55, a recombinant polypeptide identical to one of the major fragments identified in natural deposits (11). This polypeptide includes the entire variable region and a specific portion of the constant domain. The 133-AL55 truncated species maintains a globular soluble state in physiological solution, but under appropriate conditions of shear stress and concentration, is converted into insoluble amyloid fibrils, microscopically and spectroscopically similar to their *ex vivo* counterpart.

NMR spectroscopy of globular 133-AL55 reveals the high flexibility and lack of stable structure of its C-terminal tail, spanning residues 117 to 133. When subjected to biocompatible mechanical forces, as reported for other proteins (46, 47), 133-AL55 converts into fibrillar structures following a classical pattern with a lag phase and an exponential growth. Using FTIR, in particular, we have shown that *in vitro* fibrils by 133-AL55 have a parallel β-sheet configuration, consistent with what previously documented in fibrils extracted from natural deposits (16).

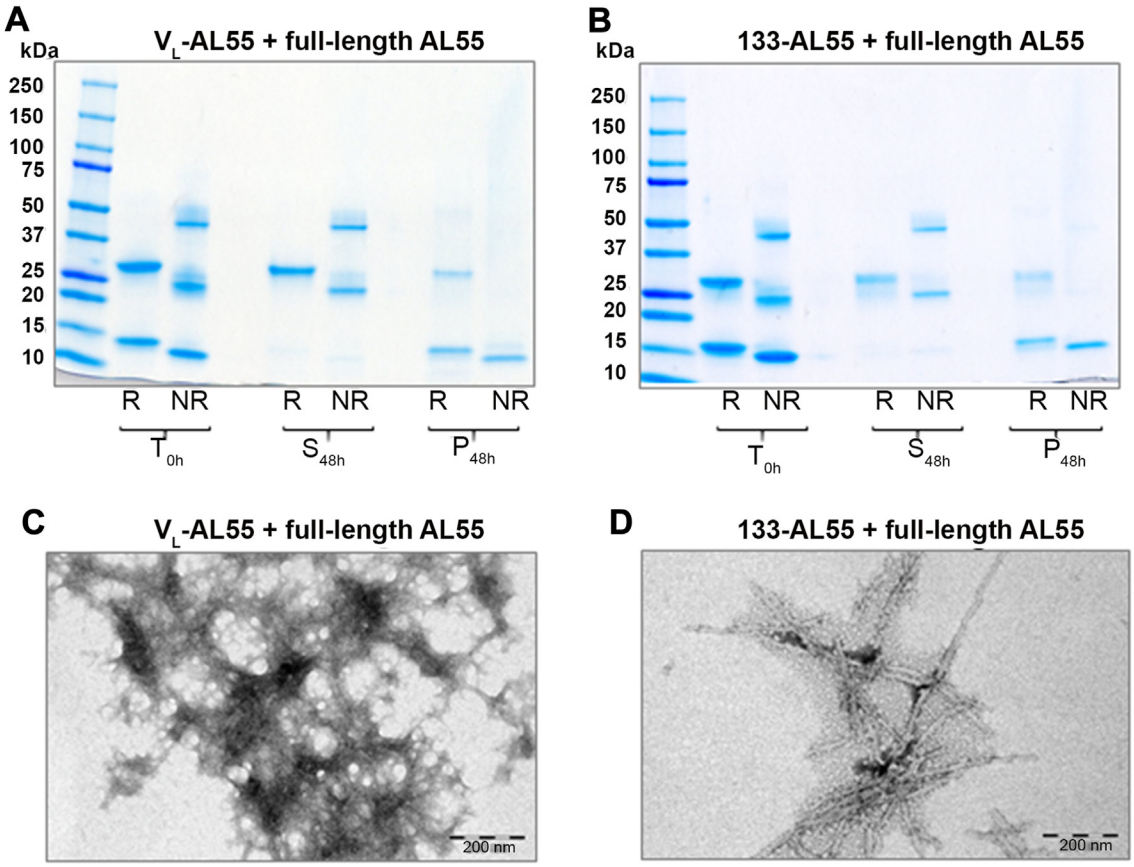

Figure 7. Electrophoretic and TEM analyses of aggregates from the fibrillogenesis of 133-AL55 or V_L-AL55 in mixture with full-length AL55. *A* and *B*, SDS 4 to 20% PAGE analysis of supernatants and pellets from the coincubation of full-length AL55 with V_L-AL55 and 133-AL55, respectively. Samples were withdrawn after 48 h of incubation; insoluble aggregates were separated by centrifugation, as detailed in Methods. Mixtures at time 0 (T_{0h}) are shown for comparison. *C* and *D*, TEM images of aggregates from the cofibrillogenesis of full-length AL55 with V_L-AL55 and 133-AL55, respectively. Samples were withdrawn after 48 h of incubation and directly applied onto the carbon grid (negative staining; the scale bars represent 200 nm). NR, nonreducing conditions; P, pellet; S, supernatant; R, reducing conditions; TEM, transmission electron microscopy; V_L, light chain's variable domain.

To our knowledge, this is the first time in which a specific truncated form of λ LC containing a portion of the C_L, suitable for making genuine amyloid fibrils *in vitro*, is studied both at the level of structure of its globular state and dynamics of fibrillar aggregation. It is otherwise well known (48), and confirmed in this study, that isolated V_L domains of amyloidogenic LCs easily form amyloid fibrils *in vitro*; however, V_L-AL55–derived fibrils lack the parallel β-strand configuration of their *ex vivo* counterpart. On the contrary, full-length LCs are extremely resistant to *in vitro* fibrillar conversion (12, 24).

In natural deposits, truncated species containing portions of the C_L, such as 133-AL55, are major components (29, 30), although the full-length and short V_L fragments are also represented. Therefore, to provide a new model mimicking the putative conditions of amyloidogenesis *in vivo*, we have explored the fibrillogenesis of mixtures of different species. The hypothesis that V_L or 133-AL55 fragments could influence and possibly prime the fibrillogenesis of the full-length LC was monitored by ThT assay and by isotope edited FTIR. ThT clearly shows that neither the V_L domain nor the 133-AL55 fragment is able to recruit the full-length LC into amyloid fibrils, at least under the biocompatible conditions here used. Moreover, we highlight a paradoxical and unexpected inhibition of the fibrillogenesis rate when the full length is incubated with 133-AL55.

Using isotope edited FTIR, we further dissect the behavior of the single species in the mix. In particular, focusing on the full-length LC, we show that it mostly does not integrate into nascent fibrils but progressively loses solubility and separately aggregates into amorphous material, especially during the fibrillar conversion of 133-AL55. Coexistence of fibrillar and amorphous aggregates is confirmed by EM analysis, and it is worth of note that, in many amyloid biopsies, an amorphous background can be visualized by EM in concomitance with ordered amyloid fibrils. Although full-length AL55 is not clearly incorporated into fibrils in the presence of the amyloidogenic fragments, we have evidence of an increased tendency of the intact precursor to precipitate as amorphous species in the presence of 133-AL55. This finding can have an impact in the long-term debate about the potential remodeling of prefibrillar ("amorphous") aggregates into fibrils *in vitro*, opening the way to future studies to investigate whether LC proteolysis occurs before or after aggregation.

Our findings also help us interpret the kinetics of amyloidogenesis *in vivo* and highlight how specific LC truncations can influence the rate of amyloid onset and growth. This work

strongly raises the issue of the relation between truncated and full-length LC species, which needs to be explored. In particular, this first information can be a useful step to further interpret a successful AL animal model, in which amyloid deposition is induced by seeds that contain abundant truncated forms (49, 50).

Experimental procedures

All chemicals were from Merck, Sigma-Aldrich, or Thermo Fisher Scientific, unless otherwise specified.

Expression and purification of recombinant full-length AL55 and fragments

Clinical phenotype and primary sequence (GenBank #MH670901) of the AL55 amyloidogenic human immunoglobulin λ LC, here used, have been previously described and extensive biochemical and structural information of the corresponding *ex vivo* fibrils was already available (11, 16, 31). Constructs of different length were designed as follows: 1) full-length AL55 (651 bp; 217 amino acids); 2) V_L (V_L-AL55), containing the variable and joining regions (333 bp, corresponding to 111 amino acids); and 3) 1 to 133 fragment (133-AL55), spanning the V_L and 22 amino acids of C_L (399 bp, 133 amino acids). Sequences were cloned (Twin Helix) in pET-29a expression vectors, between the NdeI and XhoI restriction sites, followed by transformation of *Escherichia coli* BL21(DE3) competent cells (Thermo Fisher Scientific). Protein expression was induced by addition of IPTG, incubation for 4 h at 37 °C and expressed into cytoplasmic inclusion bodies. Cells were harvested by centrifugation, washed in 0.1 M $NaHPO_3$ pH 7.4, and incubated for 30 min at 37 °C in the same buffer containing 0.1 mg/ml of chicken egg lysozyme. After centrifugation cells were sonicated in 0.1 M $NaHPO_3$, pH 7.4, 1 mM EDTA, 5 mM DTT, 1 mM PMSF, and centrifuged. Pellet containing inclusion bodies was solubilized overnight at 4 °C in 15 ml of 0.1 M $NaHPO_3$, 6 M GdnHCl, 10 mM EDTA, 5 mM DTT, 1 mM PMSF, pH 7.4 and centrifuged before proceeding to the refolding protocol which was tailored to each specific proteoform. For both full-length AL55 and 133-AL55, the protein solution was diluted dropwise (1: 20 final dilution) in ice-cold refolding buffer (0.1 M $NaHPO_3$ pH 7.4, 1 mM EDTA, 1 mM PMSF, 5 mM reduced L-glutathione, and 0.5 mM oxidized L-glutathione), followed by overnight incubation under stirring at 4 °C. Pellets were removed by centrifugation, and the refolded protein in the supernatant was dialyzed overnight against 50 mM Tris–HCl buffer, pH 8. A modified refolding procedure was required to reduce precipitation of the recombinant V_L-AL55 isoform. In this case, protein was subjected to a three-step dialysis in which GdnHCl was gradually diluted from 1 M to 0.25 M in 50 mM Tris–HCl buffer, pH 8. After refolding, proteins were subjected to a first purification step by ion exchange chromatography, using an HiPrep Q HP 16/10 (Cytiva), followed by size-exclusion chromatography on a Superdex HiLoad 16/600 75pg column. Protein concentration was determined spectrophotometrically at 280 nm using the molar extinction coefficient predicted for each isoform with the sequence-based ProtParam tool on the Expasy website (https://web.expasy.org/protparam/). Purified proteins were immediately frozen at −80 °C. Before use, all proteins were filtered through a 0.22-μm filter to remove any aggregates. For NMR and isotope-edited FTIR spectroscopy analyses, isotopically labeled [^{15}N and ^{13}C] full-length AL55 and 133-AL55 were produced as above, by growing bacteria using Spectra 9 minimal medium containing 98% ^{13}C and 98% ^{15}N (Cambridge Isotope Laboratories).

Far-UV CD and protein stability measurement

Far-UV CD spectra were recorded on a Jasco J-815 spectropolarimeter (Jasco Corp), equipped with a Peltier temperature controller, using the following conditions: 10 μM protein concentration in PBS pH 7.4, 0.1 cm path length quartz cell, 10 °C, scanning speed of 20 nm/min, 195 to 260 nm spectral range, three scans per spectrum. For thermal unfolding experiments, samples were heated from 10 °C to 85 °C at a rate of 1 °C/min and the ellipticity at 203 nm was monitored every 0.2 °C. CD spectra in the far-UV range were collected at 10 °C and 85 °C. After cooling down the sample at 10 °C, a second thermal treatment was performed on the same sample to assess the reversibility of the observed structural changes. The content in protein secondary structures was calculated from the CD spectra collected at 10 °C using the online BeStSel prediction tool (51). Three independent experiments were performed.

Fibrillogenesis and cofibrillogenesis experiments

All fibrillogenesis experiments were carried out at 37 °C in PBS pH 7.4 under agitation. Different agitation speeds (900, 300, and 100 rpm respectively) and protein concentration (from 1 to 20 μM) were tested. Amyloid fibril formation was monitored by measuring ThT emission fluorescence at 480 nm following excitation at 445 nm and using 10 μM ThT final concentration. Kinetics studies were performed in Costar 96-well black-walled plates (Corning) sealed with transparent film, on a Clariostar plate reader (BMG Labtech), with measurements at 15-min intervals. Fibrillogenesis reactions for TEM, FTIR, and SDS-PAGE analyses was performed in 1 ml glass vials (working volume: 500 μl) under magnetic stirring; in this case ThT fluorescence was measured at intervals on aliquots of the corresponding suspensions. At least three independent experiments were performed, testing overall two different batches of each unlabeled protein. For cofibrillogenesis studies, samples containing equimolar concentrations of soluble full-length AL55 and either soluble V_L-AL55 or 133-AL55 were incubated and analyzed as above using 20 μM for all experiments except for FTIR studies, in which 30 μM was used to improve the signal. In experiments requiring separation of the soluble fraction from aggregates, samples withdrawn at different time points were centrifuged at 20,800*g* for 20 min; pellets were washed in all cases with PBS and centrifuged again. To calculate T_{50} values (values of the time at which the reaction reached its midpoint fluorescence), ThT fluorescence curves were fit to asymmetric sigmoidal

equations, using GraphPad Prism version 9.4.0. Seeding and cross-seeding experiments were performed by incubating soluble proteins with preformed aggregates by either 133-AL55 or V_L-AL55. The seeds were generated by incubating 20 μM V_L-AL55 or 133-AL55 as described above, which leads to their complete conversion into insoluble aggregates. Seeds suspensions were added to solutions of 20 μM soluble proteins in a 1:10 v/v ratio, followed by incubation in microplates at 37 °C under agitation (900 rpm), in the presence of 10 mM ThT.

Sodium dodecyl sulfate polyacrylamide gel electrophoresis

Samples were diluted in SDS-PAGE buffer (62 mM Tris–HCl, 10% (v/v) glycerol, 2% (w/v) SDS, bromophenol blue), denatured for 10 min at 90 °C, and loaded on 4 to 20% Mini-protean TGX Precast gel (Bio-Rad). Addition of 1% (v/v) β-mercaptoethanol was used to separate proteins under reducing conditions. Gels were stained with colloidal Coomassie blue G-250 (Gel Code blue staining reagent, Sigma-Aldrich).

FTIR spectroscopy studies

For FTIR measurements in attenuated total reflection, 2 μl of each sample (at 30 μM of each protein in PBS buffer pH 7.4) were deposited on the diamond plate of the single reflection attenuated total reflection device (Quest, Specac). Spectra were recorded after solvent evaporation to allow the formation of a hydrated protein film, as previously reported (42, 43). The Varian 670-IR spectrometer (Varian Australia Pty Ltd), equipped with a nitrogen-cooled mercury cadmium telluride detector and an air dryer purging system, was employed under the following conditions: 2 cm^{-1} spectral resolution, 25 kHz scan speed, 1024 scan coadditions, and triangular apodization. The second derivatives of each measured spectra were obtained after Savitsky–Golay smoothing by using the Resolutions Pro software (Varian Australia Pty Ltd). At least three independent experiments were performed.

NMR spectroscopy

NMR spectra were acquired on a 700 MHz AVANCE NEO spectrometer (Bruker Biospin) equipped with a triple-resonance cryoprobe. The uniformly [^{13}C, ^{15}N]-labeled recombinant 133-AL55 was dissolved in a mixture 95/5 vol/vol PBS buffer pH 7.4/D_2O to reach a 0.5 mM protein concentration. A series of 2D [^1H-^{15}N] HSQC spectra were acquired at 37 °C along 12 h to monitor the conformational stability of the 133-AL55 fragment. Partial assignment of backbone resonances was obtained for a second 133-AL55 sample in the same buffer and concentration conditions, but at a temperature of 15 °C. The assignment was based on three-dimensional HNCA, HNCOCA, HNCACB, HNCO, and HNCACO experiments (52). Backbone dynamics of 133-AL55 in solution was investigated by ^1H-^{15}N heteronuclear NOE (^1H-^{15}N NOE). The [^1H-^{15}N] correlation spectra were recorded in the presence and absence of ^1H saturation (giving rise to NOE and NO-NOE spectra, respectively). The intensity ratio (NOE/NO-NOE) was used to determine residue-specific ^1H-^{15}N NOE values for each detected peak. Experiments were collected using the pulse program *hsqcnoef3gpsi3d* from the Bruker library (Topspin, version 4.1.4); the relaxation delay was set to 5 s and the total acquisition time to 3 h, respectively. Spectra were processed with Topspin 4.1.4 (Bruker Biospin) and analyzed in NMRFAM-SPARKY 3.115 (53). The structure of the three proteoforms was also predicted in silico by DeepMind AlphaFold2 software (https://alphafold.ebi.ac.uk/) (36, 54).

Transmission electron microscopy

TEM samples were prepared by applying 20 μl of each unpelleted sample (diluted 1:10 with ultrapure water) onto a 200-mesh carbon-coated Formvar nickel grid (Electron Microscopy Sciences) and allowed to sediment on the carbon film for 2 min, followed by negative staining with a 5% (w/v) uranyl acetate solution for 1 min. Excess solutions were removed with filter paper. Samples were imaged with a JEOL JEM-1011 transmission electron microscope (Jeol) at 80 kV. All representative TEM micrographs in this publication have been chosen from 5 to 20 images.

Statistics

The number of replicates is indicated in each experimental section. Differences in mean values were determined by two-tailed Student's t test for independent samples and considered statistically significant when p values were < 0.05.

Data availability

Data generated in this study are contained within the manuscript and associated supporting information.

Supporting information—This article contains supporting information.

Acknowledgments—V. B. is Emeritus Professor of Medical Biochemistry at University College London, London. We wish to thank Centro Grandi Strumenti (CGS) of University of Pavia for providing access to NMR instrumentation.

Author contributions—F. L., V. B., and S. G. conceptualization; F. L. and S. G. supervision; F. L., A. N., and S. G. writing-original draft; A. N., L. M., D. A., A. C., S. R., M. C. M., S. M., P. P. M., M. T. P., A. L., and M. C. investigation; A. N., L. M., D. A., A. C., G. V., and D. C. formal analysis; L. M., P. P. M., and E. A. validation; P. P. M. data curation; G. V. software; V. B. and S. G. conceptualization; S. G. supervision; F. L., A. N., L. M., D. A., A. C., S. R., M. C. M., S. M., P. P. M., M. T. P., A. L., M. C., G. V., D. C., E. A., V. B., and S. G. writing-review and editing.

Funding and additional information—This grant was supported by the following grants: Cariplo–Telethon Joint Call for Applications (2022-0578), Cariplo grant 2022-0535, the Italian Ministry of Research and University "Dipartimenti di Eccellenza" 2018–2022 and 2023–2027 grants to the Molecular Medicine Department (University of Pavia), and PNRR grant National Center for Gene Therapy and Drugs based on RNA Technology ID MUR: CN00000041.

Conflict of interest—The authors declare that they have no conflicts of interest with the contents of this article.

Abbreviations—The abbreviations used are: C_L, light chain's constant domain; EM, electron microscopy; HSQC, heteronuclear single quantum coherence; LC, light chain; TEM, transmission electron microscopy; ThT, Thioflavin T; V_L, light chain's variable domain.

References

1. Buxbaum, J. N., Dispenzieri, A., Eisenberg, D. S., Fändrich, M., Merlini, G., Saraiva, M. J. M., *et al.* (2022) Amyloid nomenclature 2022: update, novel proteins, and recommendations by the international society of amyloidosis (ISA) nomenclature committee. *Amyloid* **29**, 213–219
2. Merlini, G., Dispenzieri, A., Sanchorawala, V., Schönland, S. O., Palladini, G., Hawkins, P. N., *et al.* (2018) Systemic immunoglobulin light chain amyloidosis. *Nat. Rev. Dis. Primers* **4**, 38
3. Bellotti, V., Mangione, P., and Merlini, G. (2000) Review: immunoglobulin light chain amyloidosis–the archetype of structural and pathogenic variability. *J. Struct. Biol.* **130**, 280–289
4. Kourelis, T. V., Dasari, S., Theis, J. D., Ramirez-Alvarado, M., Kurtin, P. J., Gertz, M. A., *et al.* (2017) Clarifying immunoglobulin gene usage in systemic and localized immunoglobulin light-chain amyloidosis by mass spectrometry. *Blood* **129**, 299–306
5. Kyle, R. A., and Greipp, P. R. (1982) "Idiopathic" Bence Jones proteinuria: long-term follow-up in seven patients. *N. Engl. J. Med.* **306**, 564–567
6. Del Pozo-Yauner, L., Herrera, G. A., Perez Carreon, J. I., Turbat-Herrera, E. A., Rodriguez-Alvarez, F. J., and Ruiz Zamora, R. A. (2023) Role of the mechanisms for antibody repertoire diversification in monoclonal light chain deposition disorders: when a friend becomes foe. *Front. Immunol.* **14**, 1203425
7. Bodi, K., Prokaeva, T., Spencer, B., Eberhard, M., Connors, L. H., and Seldin, D. C. (2009) AL-Base: a visual platform analysis tool for the study of amyloidogenic immunoglobulin light chain sequences. *Amyloid* **16**, 1–8
8. Palladini, G., and Merlini, G. (2022) How I treat AL amyloidosis. *Blood* **139**, 2918–2930
9. Sternke-Hoffmann, R., Pauly, T., Norrild, R. K., Hansen, J., Tucholski, F., Høie, M. H., *et al.* (2023) Widespread amyloidogenicity potential of multiple myeloma patient-derived immunoglobulin light chains. *BMC Biol.* **21**, 21
10. Oberti, L., Rognoni, P., Barbiroli, A., Lavatelli, F., Russo, R., Maritan, M., *et al.* (2017) Concurrent structural and biophysical traits link with immunoglobulin light chains amyloid propensity. *Sci. Rep.* **7**, 16809
11. Lavatelli, F., Mazzini, G., Ricagno, S., Iavarone, F., Rognoni, P., Milani, P., *et al.* (2020) Mass spectrometry characterization of light chain fragmentation sites in cardiac AL amyloidosis: insights into the timing of proteolysis. *J. Biol. Chem.* **295**, 16572–16584
12. Morgan, G. J., and Kelly, J. W. (2016) The kinetic stability of a full-length antibody light chain dimer determines whether endoproteolysis can release amyloidogenic variable domains. *J. Mol. Biol.* **428**, 4280–4297
13. Morgan, G. J., Usher, G. A., and Kelly, J. W. (2017) Incomplete refolding of antibody light chains to non-native, protease-sensitive conformations leads to aggregation: a mechanism of amyloidogenesis in patients? *Biochemistry* **56**, 6597–6614
14. Eulitz, M. (1992) Amyloid formation from immunoglobulin chains. *Biol. Chem. Hoppe Seyler* **373**, 629–633
15. Absmeier, R. M., Rottenaicher, G. J., Svilenov, H. L., Kazman, P., and Buchner, J. (2023) Antibodies gone bad - the molecular mechanism of light chain amyloidosis. *FEBS J.* **290**, 1398–1419
16. Swuec, P., Lavatelli, F., Tasaki, M., Paissoni, C., Rognoni, P., Maritan, M., *et al.* (2019) Cryo-EM structure of cardiac amyloid fibrils from an immunoglobulin light chain AL amyloidosis patient. *Nat. Commun.* **10**, 1269
17. Radamaker, L., Baur, J., Huhn, S., Haupt, C., Hegenbart, U., Schönland, S., *et al.* (2021) Cryo-EM reveals structural breaks in a patient-derived amyloid fibril from systemic AL amyloidosis. *Nat. Commun.* **12**, 875
18. Radamaker, L., Karimi-Farsijani, S., Andreotti, G., Baur, J., Neumann, M., Schreiner, S., *et al.* (2021) Role of mutations and post-translational modifications in systemic AL amyloidosis studied by cryo-EM. *Nat. Commun.* **12**, 6434
19. Kazman, P., Absmeier, R. M., Engelhardt, H., and Buchner, J. (2021) Dissection of the amyloid formation pathway in AL amyloidosis. *Nat. Commun.* **12**, 6516
20. Rottenaicher, G. J., Weber, B., Rührnößl, F., Kazman, P., Absmeier, R. M., Hitzenberger, M., *et al.* (2021) Molecular mechanism of amyloidogenic mutations in hypervariable regions of antibody light chains. *J. Biol. Chem.* **296**, 100334
21. Brumshtein, B., Esswein, S. R., Landau, M., Ryan, C. M., Whitelegge, J. P., Phillips, M. L., *et al.* (2014) Formation of amyloid fibers by monomeric light chain variable domains. *J. Biol. Chem.* **289**, 27513–27525
22. Ruiz-Zamora, R. A., Guillaumé, S., Al-Hilaly, Y. K., Al-Garawi, Z., Rodríguez-Alvarez, F. J., Zavala-Padilla, G., *et al.* (2019) The CDR1 and other regions of immunoglobulin light chains are hot spots for amyloid aggregation. *Sci. Rep.* **9**, 3123
23. Misra, P., Blancas-Mejia, L. M., and Ramirez-Alvarado, M. (2019) Mechanistic insights into the early events in the aggregation of immunoglobulin light chains. *Biochemistry* **58**, 3155–3168
24. Rottenaicher, G. J., Absmeier, R. M., Meier, L., Zacharias, M., and Buchner, J. (2023) A constant domain mutation in a patient-derived antibody light chain reveals principles of AL amyloidosis. *Commun. Biol.* **6**, 209
25. Klimtchuk, E. S., Gursky, O., Patel, R. S., Laporte, K. L., Connors, L. H., Skinner, M., *et al.* (2010) The critical role of the constant region in thermal stability and aggregation of amyloidogenic immunoglobulin light chain. *Biochemistry* **49**, 9848–9857
26. Rennella, E., Morgan, G. J., Kelly, J. W., and Kay, L. E. (2019) Role of domain interactions in the aggregation of full-length immunoglobulin light chains. *Proc. Natl. Acad. Sci. U. S. A.* **116**, 854–863
27. Maritan, M., Romeo, M., Oberti, L., Sormanni, P., Tasaki, M., Russo, R., *et al.* (2020) Inherent biophysical properties modulate the toxicity of soluble amyloidogenic light chains. *J. Mol. Biol.* **432**, 845–860
28. Dasari, S., Theis, J. D., Vrana, J. A., Rech, K. L., Dao, L. N., Howard, M. T., *et al.* (2020) Amyloid typing by mass spectrometry in clinical practice: a comprehensive review of 16,175 samples. *Mayo Clin. Proc.* **95**, 1852–1864
29. Lavatelli, F., Perlman, D. H., Spencer, B., Prokaeva, T., McComb, M. E., Théberge, R., *et al.* (2008) Amyloidogenic and associated proteins in systemic amyloidosis proteome of adipose tissue. *Mol. Cell Proteomics* **7**, 1570–1583
30. Enqvist, S., Sletten, K., and Westermark, P. (2009) Fibril protein fragmentation pattern in systemic AL-amyloidosis. *J. Pathol.* **219**, 473–480
31. Mazzini, G., Ricagno, S., Caminito, S., Rognoni, P., Milani, P., Nuvolone, M., *et al.* (2022) Protease-sensitive regions in amyloid light chains: what a common pattern of fragmentation across organs suggests about aggregation. *FEBS J.* **289**, 494–506
32. Brumshtein, B., Esswein, S. R., Sawaya, M. R., Rosenberg, G., Ly, A. T., Landau, M., *et al.* (2018) Identification of two principal amyloid-driving segments in variable domains of Ig light chains in systemic light-chain amyloidosis. *J. Biol. Chem.* **293**, 19659–19671
33. González-Andrade, M., Becerril-Luján, B., Sánchez-López, R., Ceceña-Álvarez, H., Pérez-Carreón, J. I., Ortiz, E., *et al.* (2013) Mutational and genetic determinants of λ6 light chain amyloidogenesis. *FEBS J.* **280**, 6173–6183
34. Blancas-Mejia, L. M., Misra, P., Dick, C. J., Cooper, S. A., Redhage, K. R., Bergman, M. R., *et al.* (2018) Immunoglobulin light chain amyloid aggregation. *Chem. Commun.* **54**, 10664–10674
35. Rennella, E., Morgan, G. J., Yan, N., Kelly, J. W., and Kay, L. E. (2019) The role of protein thermodynamics and primary structure in fibrillogenesis of variable domains from immunoglobulin light chains. *J. Am. Chem. Soc.* **141**, 13562–13571
36. Varadi, M., Anyango, S., Deshpande, M., Nair, S., Natassia, C., Yordanova, G., *et al.* (2022) AlphaFold Protein Structure Database: massively expanding the structural coverage of protein-sequence space with high-accuracy models. *Nucleic Acids Res.* **50**, D439–D444
37. Kay, L. E., Torchia, D. A., and Bax, A. (1989) Backbone dynamics of proteins as studied by 15N inverse detected heteronuclear NMR

spectroscopy: application to staphylococcal nuclease. *Biochemistry* **28**, 8972–8979
38. Barth, A. (2007) Infrared spectroscopy of proteins. *Biochim. Biophys. Acta* **1767**, 1073–1101
39. Ami, D., Mereghetti, P., and Natalello, A. (2022) Contribution of infrared spectroscopy to the understanding of amyloid protein aggregation in complex systems. *Front. Mol. Biosci.* **9**, 822852
40. Zandomeneghi, G., Krebs, M. R., McCammon, M. G., and Fändrich, M. (2004) FTIR reveals structural differences between native beta-sheet proteins and amyloid fibrils. *Protein Sci.* **13**, 3314–3321
41. Ami, D., Lavatelli, F., Rognoni, P., Palladini, G., Raimondi, S., Giorgetti, S., *et al.* (2016) *In situ* characterization of protein aggregates in human tissues affected by light chain amyloidosis: a FTIR microspectroscopy study. *Sci. Rep.* **6**, 29096
42. Natalello, A., Mangione, P. P., Giorgetti, S., Porcari, R., Marchese, L., Zorzoli, I., *et al.* (2016) Co-fibrillogenesis of wild-type and D76N β2-microglobulin: the crucial role of fibrillar seeds. *J. Biol. Chem.* **291**, 9678–9689
43. Ami, D., and Natalello, A. (2022) Characterization of the conformational properties of soluble and insoluble proteins by Fourier transform infrared spectroscopy. *Methods Mol. Biol.* **2406**, 439–454
44. Sarroukh, R., Goormaghtigh, E., Ruysschaert, J. M., and Raussens, V. (2013) ATR-FTIR: a "rejuvenated" tool to investigate amyloid proteins. *Biochim. Biophys. Acta* **1828**, 2328–2338
45. Faravelli, G., Mondani, V., Mangione, P. P., Raimondi, S., Marchese, L., Lavatelli, F., *et al.* (2022) Amyloid Formation by globular proteins: the need to narrow the gap between in vitro and in vivo mechanisms. *Front. Mol. Biosci.* **9**, 830006
46. Marcoux, J., Mangione, P. P., Porcari, R., Degiacomi, M. T., Verona, G., Taylor, G. W., *et al.* (2015) A novel mechano-enzymatic cleavage mechanism underlies transthyretin amyloidogenesis. *EMBO Mol. Med.* **7**, 1337–1349
47. Valleix, S., Gillmore, J. D., Bridoux, F., Mangione, P. P., Dogan, A., Nedelec, B., *et al.* (2012) Hereditary systemic amyloidosis due to Asp76Asn variant β2-microglobulin. *N. Engl. J. Med.* **366**, 2276–2283
48. Hurle, M. R., Helms, L. R., Li, L., Chan, W., and Wetzel, R. (1994) A role for destabilizing amino acid replacements in light-chain amyloidosis. *Proc. Natl. Acad. Sci. U. S. A.* **91**, 5446–5450
49. Martinez-Rivas, G., Ayala, M., Bender, S., Roussel, M., Jaccard, A., Bridoux, F., *et al.* (2021) A transgenic mouse model of cardiac AL amyloidosis. *Blood* **138**, Supplement 1, 1592
50. Martinez-Rivas, G., Bender, S., and Sirac, C. (2022) Understanding AL amyloidosis with a little help from in vivo models. *Front. Immunol.* **13**, 1008449
51. Micsonai, A., Moussong, É., Wien, F., Boros, E., Vadászi, H., Murvai, N., *et al.* (2022) BeStSel: webserver for secondary structure and fold prediction for protein CD spectroscopy. *Nucleic Acids Res.* **50**, W90–98
52. Sattler, M., Schleucher, J., and Christian, G. (1999) Heteronuclear multidimensional NMR experiments for the structure determination of proteins in solution employing pulsed field gradients. *Prog Nucl Magn Reson Spectrosc* **34**, 93–158
53. Lee, W., Tonelli, M., and Markley, J. L. (2015) NMRFAM-SPARKY: enhanced software for biomolecular NMR spectroscopy. *Bioinformatics* **31**, 1325–1327
54. Jumper, J., Evans, R., Pritzel, A., Green, T., Figurnov, M., Ronneberger, O., *et al.* (2021) Highly accurate protein structure prediction with AlphaFold. *Nature* **596**, 583–589